Inferring the Shallow Layered Structure at the Chang'E-4 Landing Site: A Novel Interpretation Approach Using Lunar Penetrating Radar

Iraklis Giannakis[1], Feng Zhou[2], Craig Warren[3], Antonios Giannopoulos[4]

[1]I. Giannakis is with the School of Geosciences, University of Aberdeen, Meston Building, Kings College, Aberdeen, UK, AB24 3FX. E-mail: iraklis.giannakis@abdn.ac.uk
[2]F. Zhou is with the China University of Geosciences (Wuhan), School of Mechanical Engineering and Electronic Information, Wuhan, China, 388 Lumo Rd, 430074. E-mail: zhoufeng@cug.edu.cn
[3]C. Warren is with the Department of Mechanical and Construction Engineering, Northumbria University, Newcastle, UK, NE1 8ST, E-mail: craig.warren@northumbria.ac.uk
[4]A. Giannopoulos is with the School of Engineering, The University of Edinburgh, Edinburgh, EH9 3FG, UK. E-mail: a.giannopoulos@ed.ac.uk

Key Points:

- We suggest a novel hyperbola-fitting technique that assumes an arbitrary permittivity distribution with respect to depth
- The proposed method is used to map the lunar regolith at the Chang'E-4 landing site
- A layered structure is revealed at the first 10 meters. A new stratigraphic model is suggested for the Von K*árm*á*n* crater

Corresponding author: 1, iraklis.giannakis@abdn.ac.uk

Abstract

The current paper investigates the shallow layers of the lunar regolith at the Chang'E-4 landing site. Four layers between 0-10 meters were identified using lunar penetrating radar. Based on these outputs, a revised stratigraphic model is suggested for the post-Imbrian ejecta at the Von Kármán crater. The layers were previously unseen due to the smooth boundaries between them. The revised model was inferred using an advanced hyperbola-fitting scheme. Applying conventional hyperbola-fitting to non-homogeneous media results in errors and inaccuracies that are often wrongly assumed to be negligible. We propose a novel hyperbola-fitting scheme that is not constrained to homogeneous media and can be applied subject to any arbitrary one-dimensional permittivity distribution. Via this approach, we can estimate the permittivity profile of an investigated area and detect layered structures that were previously transparent to electromagnetic waves due to the gradational dielectric properties at their interfaces.

Plain Language Summary

The landing site of Cheng'E-4 is at the Von Kármán (VK) crater at the South Pole-Aitken (SPA) basin. SPA is the oldest and biggest basin on the Moon created at the early stages of its evolution by an impact that is believed that has penetrated the lunar crust and uplifted materials from the top mantle. Understanding the geology and stratigraphy of SPA can help us understand cratering processes and shed a light on the evolution of the Moon. In the current paper, we have used lunar penetrating radar data from the Chang'E-4 mission combined with a novel interpretation tool to reveal a previously unseen layered structure for the first ~ 10 m of the VK crater.

Keywords

South-Pole Aitken (SPA), Chang'E-4, Lunar Penetrating Radar (LPR), Ground Penetrating Radar (GPR), hyperbola-fitting.

1 Introduction

Ground penetrating radar (GPR) is a mature geophysical technique (Daniels, 2004) with a unique span of applications ranging from landmine detection (Feng et al., 2012; Giannakis et al., 2016) and concrete inspection (Wai-Lok Lai et al., 2018; Giannakis et al., 2020), to glaciology (Williams et al., 2014) and archaeology (Conyers, 2004). In planetary sciences, GPR has been applied both for satellite (Lauro et al., 2020) and in-situ measurements (Li et al., 2020), with promising results for mapping sub-glacial water bodies in Mars (Lauro et al., 2020), and for inferring the layered structure of the lunar regolith (Lai et al., 2020; Li et al., 2020; Zhang et al., 2020).

Subject to the application and the employed measurement configuration, various GPR processing and interpretation techniques have been suggested over the years (Daniels, 2004). From typical signal processing (Li et al., 2015; Cassidy, 2009) and linear Born approximations (Boero et al., 2018), to machine learning (Giannakis et al., 2019) and full-waveform inversion (Meles et al., 2010). Within that context, hyperbola-fitting is considered one of the most mainstream techniques for the interpretation of common-offset GPR data (Mertens et al., 2016). The simplicity and computational efficiency of hyperbola-fitting make it an appealing choice for mapping the dielectric properties of an investigated medium, and for estimating the coordinates of subsurface targets (Mertens et al., 2016).

Hyperbola-fitting has been used in both Chang'E-3 and Chang'E-4 missions (Li et al., 2020; Fa, 2020; Dong, Fang, et al., 2020; Dong, Feng, et al., 2020; Lai et al., 2019) for estimating the electric permittivity of lunar regolith and subsequently inferring its

density and mineralogical composition (Dong, Feng, et al., 2020; Li et al., 2020). Nonetheless, the underlying assumptions of hyperbola-fitting constrain its applicability, especially in complex environments where permittivity varies with depth. To mitigate that, conventional hyperbola-fitting is often complemented with Dix conversion (Dix, 1955; Dong, Fang, et al., 2020) in order to transform the estimated bulk velocity to actual velocity. Through a series of numerical examples, it is illustrated that this approach (Dong, Fang, et al., 2020) has limited applicability for the lunar regolith and should be used with caution. To that extent, we present a novel hyperbola-fitting that tackles this problem by simultaneously fitting multiple hyperbolas subject to any arbitrary 1D permittivity distribution.

The proposed scheme is applied to the Lunar Penetrating Radar (LPR) data collected by the Yutu-2 rover during the first two lunar days of the Chang'E-4 mission at the Von K*árm*á*n* (VK) crater (Li et al., 2020). Four distinct layers –that were previously not visible due to the smooth boundaries between them– were identified within the first 10 m. This outcome differs significantly from previous theories suggesting that the first 12 m of the landing site are fairly homogeneous, part of the weathered fine-grained regolith that lies on top of the ejecta from the Finsen crater (Zhang et al., 2020). Based on the revised permittivity profile and the available literature on the geology of the Chang'E-4 landing site, we suggest a new post-Imbrian stratigraphic model for the VK crater, in which an approximately $\sim$ 3 m weathered fine-grained layer is followed by $\sim$ $8-10$ meters of ejecta from the VK L and L' craters overlaying the ejecta from the Finsen crater.

2 The Chang'E-4 Landing Site

The Chinese lunar probe Chang'E-4, carrying the Yutu-2 rover, was the first human-made object that landed on the far-side of the Moon on 3rd of January 2019 (Li et al., 2019; Tang et al., 2020). The landing site is located at the South Pole-Aitkens (SPA) basin – the oldest and biggest crater on the Moon (Huang et al., 2018; Hu et al., 2019; James et al., 2019). The SPA basin is pre-Nectarian in age and has an elliptical shape with an approximate diameter of 2100-2500 km (Moriarty et al., 2013). The transient cavity of the SPA basin has been estimated between 840-1400 km (Potter et al., 2012; Moriarty et al., 2013). The maximum excavation depth of lunar craters is approximately 10 % of their diameter (Stopar et al., 2017), which implies that the SPA basin excavated up to 140 km through the lunar crust and into the mantle (Moriarty et al., 2013). This premise is based on the maximum width of lunar crust $\sim$ 60 km, as estimated by the Gravity Recovery and Interior Laboratory (GRAIL) mission (Wieczorek et al., 2013), which is in good agreement with seismic data from the Apollo missions (Khan, 2002). The shallow mantle layer was most-likely melted during the impact (Moriarty et al., 2013) and parts of it are expected to occur within the SPA basin, forming an underlying sheet of non-crustal materials (Potter et al., 2012; Moriarty et al., 2013). These materials are of paramount importance since they can constrain the composition of the upper mantle and provide an insight into the early evolution of the Moon (Moriarty et al., 2013).

Based on previous models of lunar evolution –that suggest an upper mantle predominantly composed of olivine (Yamamoto et al., 2010)– strong spectral signatures of olivine were expected to be present within the SPA crater (Ivanov et al., 2018). Nonetheless, data from CLEMENTINE and SELENE did not support this premise (Tompkins & Pieters, 1999; Matsunaga et al., 2008; Yamamoto et al., 2010), apart from small occurrences of olivine clusters (Yamamoto et al., 2010) most likely originated from crustal materials, due to their location (the exterior of the SPA) and the high content of feldspar in their near proximity (Moriarty & Pieters, 2018). The SPA is dominated by mafic materials and in particular with Mg-rich and low-Ca pyroxene (Moriarty & Pieters, 2018). CLEMENTINE measurements reveal an inner zone with Fe abundance and an outer zone with lower Fe content (Jolliff et al., 2000). Furthermore, using data from the Moon Mineralogy Mapper (M^3), Moriarty & Pieters 2018 have divided the SPA into four zones. The

first zone is the inner SPA area called SPACA, with characteristic Ca-pyroxene abundance that lies at the center of the SPA. The second zone surrounds SPACA, and it is an area with Mg-rich pyroxenes. Based on spectral analysis of the central peaks of the craters within SPACA, strong indications were given to support the premise that SPACA lays on top of the Mg-rich area (Moriarty & Pieters, 2018). The third zone is a heterogeneous anulus that consists of pyroxene and feldspar, and acts as the intermediate stage between the SPA and its exterior. The latter is the fourth zone, a mafic-free area with high content of feldspar, similar to lunar highlands (Moriarty & Pieters, 2018).

The landing site of Chang'E-4 is within the Mg-rich anulus and in particular in the interior of the VK crater (177.588°E, 45.4578°S). VK is an elliptical crater (Zhang et al., 2020) with approximately ~ 186 km diameter (Huang et al., 2018). The age of VK was estimated pre-Nektarian (Huang et al., 2018) and recent studies have placed it at $\tilde{4}.2$ Ga (Lu et al., 2021), very close to the formation of SPA (Lu et al., 2021). The creation of Leibnitz crater affected the north part of VK and contributed to the ejecta layer prior to the Imbrian basaltic flood (Huang et al., 2018). Ejecta from Alder crater (dated at $\tilde{3}.5$ Ga (Lu et al., 2021)) are also expected to the pre-basaltic layers (Huang et al., 2018). The VK crater was flooded with basalts during the Imbrian period (Paskert et al., 2018) around $\tilde{3}.2-3.3$ Ga. Subsequently, ejecta from the Finsen crater were deposited at the end of Imbrian and early Eratosthenian ($\tilde{3}.1$ Ga (Lu et al., 2021)). Recent studies suggest that Orientale crater might have added to the post-Imbriun VK layers as well (Xiao et al., 2021). Subsequently, the Eratosthenian craters VK L and L' were formed (Zhang et al., 2020). The VK, Leibnitz, Alder, VK L, and L' lay within the Mg-pyroxene anulus while Finsen is within SPACA (Moriarty & Pieters, 2018).

Geological context suggests that the craters VK L, L', Finsen and Orientale have contributed to most of the post-Imbrian ejecta layers of the VK crater (Huang et al., 2018; Di et al., 2019; Xiao et al., 2021). The size of the ejecta from the Finsen crater is estimated –via numerical simulations (Di et al., 2019)– at ~ 30 meters. This is not in good agreement with the results obtained using dark-halo and non-dark halo craters (Li et al., 2020) that suggest a thicker post-basaltic layer, probably due to the presence of Orientale ejecta (Xiao et al., 2021). Nonetheless, contradicting data (Yue et al., 2020) place the date of Orientale to be older than the Imbrian basaltic flood, which implies that there might be another source that contributed to the post-basaltic VK layers.

The surface of the landing site is smooth with a small amount of boulders, most of them being glassy fragments and breccias from secondary craters (Lin et al., 2020). From in situ reflectance data, the visible surface at the landing site is not olivine-pyroxene rich and consists of 56-72% plagioclase, similar to lunar highlands (Hu et al., 2019; Li et al., 2019) with Mg-rich orthopyroxene (Gou et al., 2020). The thickness of the regolith (weathered top soil) is estimated using LROC NAC images at $\sim 2.5 - 7.5$ m (Huang et al., 2018). Based on the M^3 reflectance data, it is estimated that below the top weathered soil, lays a low-calcium pyroxene (LCP) layer ranging from $\sim 8 - 13$ m followed by a high-calcium pyroxene (HCP) layer from $\sim 13 - 53$ m (Huang et al., 2018). Below that, the Imbrian basalt deposits are expected to overlay the ejecta from the Alder and Leibnitz craters on top of the brecciated bedrock from the VK impact (Huang et al., 2018).

Further insights on the ejecta at the VK crater are provided by the LPR mounted to the Yutu-2 rover of the Chang'E-4 mission (Li et al., 2020). The first attempt to examine the lunar surface with in-situ LPR equipment occurred during the Chang'E-3 mission on the near side of the moon (Lai et al., 2019). Similar antenna configurations were employed for both Chang'E-3 and Chang'E-4 missions (Li et al., 2020). In particular, two antennas with 500 MHz central frequency (at the bottom of the rover), and one low frequency antenna (mounted at the back of the rover) with 60 MHz central frequency (Li et al., 2020). The low frequency antenna in the Chang'E-4 mission gave thin indications of four different lava flows that probably occurred during the Imbrian period (Lai

et al., 2020). Unfortunately, the low frequency data in both missions suffer from ringing noise due to the coupling between the antenna and the rover, which resulted in erroneous reflections and noisy data (Li et al., 2018; Zhang et al., 2020). In contrast to the Chang'E-3 landing site (Lai et al., 2019), in the VK crater, the ilmenite content is fairly low, making the ejecta layers transparent to LPR (Dong, Fang, et al., 2020). This resulted in good quality data that clearly demonstrated a complex layered structure for the first 50 meters of the VK crater (Zhang et al., 2020; Li et al., 2020). In addition, using a conventional hyperbola-fitting (assuming a homogeneous medium) with Dix conversion, the electric permittivity of the ejecta layers was estimated, and furthermore used to infer the mineralogical (Fe and Ti content) (Li et al., 2020) and the mechanical (density) properties of the lunar regolith (Dong, Fang, et al., 2020; Dong, Feng, et al., 2020), based on semi-empirical formulas fine-tuned for lunar soils (Olhoeft & Strangway, 1975; Carrier et al., 1991; Hickson et al., 2018). The relative electric permittivity at the landing site monotonically increases from $\sim 3-6$ with respect to depth, as estimated using typical hyperbola fitting (Dong, Fang, et al., 2020). This corresponds to a density that starts from $\sim 1\ gr/cm^3$ at the surface and reaches $2.5\ gr/cm^3$ at 50 m depth (Dong, Fang, et al., 2020).

3 Methodology

3.1 Advanced hyperbola-fitting

In this section, a novel hyperbola-fitting framework is described, capable of dealing with half-spaces with arbitrary 1D permittivity distributions $\epsilon(y)$ (see Figure 1). Similar to typical hyperbola-fitting, in order to avoid non-uniqueness (Mertens et al., 2016; Giannakis et al., 2019), the proposed scheme assumes that the radius (R) of the investigated target equals with zero. Subject to a varying velocity with depth, the two way travel time t that it takes for the wave to travel from the point $\overrightarrow{B} = \langle x, y\rangle$ to the point $\overrightarrow{A} = \langle x_0, d\rangle$ via the parametric curve $\overrightarrow{q}(m) = \langle q_x(m), q_z(m)\rangle$ (where $m \in [0-1]$ and d is the depth of the target) can be calculated using a scalar line integral over $\overrightarrow{q}(m)$

$$t = \frac{2}{c_0}\int_0^1 \sqrt{\epsilon(y)}\,||\frac{\partial \overrightarrow{q}(m)}{\partial m}||dm. \tag{1}$$

Given a specific velocity structure, the path $\overrightarrow{q}(m)$ can be calculated using Fermat's principle (Aldo, 1996). The notation $||\frac{\partial \overrightarrow{q}(m)}{\partial m}||$ is used to denote the norm of the first derivative of the parametric curve $\overrightarrow{q}(m)$ with respect to the parameter $m \in [0{-}1]$. It is shown that if we simplify equation (1) and make the assumption that the path $\overrightarrow{q}(m)$ is the straight line that connects the antenna to the center of the target, it leads to an elegant and computationally efficient formulation without compromising accuracy (more details are given in 3.2). The straight line that connects the antenna to the target can be expressed via the parametric curve $\overrightarrow{q}(m) = \overrightarrow{A} + \left(\overrightarrow{B} - \overrightarrow{A}\right) m$. Substituting this into equation (1) results in

$$t = \frac{2||\overrightarrow{B} - \overrightarrow{A}||}{c_0}\int_0^1 \sqrt{\epsilon(y)}dm. \tag{2}$$

The linear path of the integral in equation (2) can be written as $\overrightarrow{q}(m) = \langle x_i + m\,(x_0 - x_i)\,, y_i + m\,(d - y_i)\rangle$, where x_i, y_i are the coordinates of the antenna at the ith position. Consequently, the y variable in equation (2) can be substituted by $y = y_i + m\,(d - y_i)$, which implies that $\partial m = \frac{\partial y}{d}$ and that $y = d$ for $m = 1$. Therefore, equation (2) can be rewritten as

$$t = \frac{2||\overrightarrow{B} - \overrightarrow{A}||}{c_0 d}\int_0^d \sqrt{\epsilon(y)}dy. \tag{3}$$

Solving the integral numerically yields

$$t \approx \frac{2||\overrightarrow{B} - \overrightarrow{A}||}{c_0 d}\sum_{s=0}^{Q} \sqrt{\epsilon(s\cdot\Delta y)}\Delta y \tag{4}$$

where Δy is the discretization step and $Q = d/\Delta y$. Notice that the summation term $N(d,\epsilon) = \sum_{s=0}^{Q} \sqrt{\epsilon(s \cdot \Delta y)}\Delta y$ is independent of the position of the antenna and needs to be calculated just once. The final formulation for the proposed scheme is given by

$$t \approx \frac{2||\overrightarrow{B} - \overrightarrow{A}||}{c_0 d} N(d,\epsilon), \tag{5}$$

where the only unknowns are the permittivity function $\epsilon(y)$ and the depth of the target d. The parameter x_0 can be easily derived from the apex of the hyperbola at the measured B-Scan. Subject to a given $\epsilon(y)$, the depth of the target is calculated using the apex of the hyperbola (x_0, t_0), where $||\overrightarrow{B} - \overrightarrow{A}|| = d$

$$t_0 \approx \frac{2}{c_0} N(d,\epsilon). \tag{6}$$

For a given $\epsilon(y)$, the only unknown in equation (6) is the depth d that is estimated numerically using the bisection method. Notice that both equation (6) and the summation $N(d,\epsilon)$ in equation (4) need to be evaluated just once. The only term in equation (5) that needs to be updated as the scan progresses is the distance $||\overrightarrow{B} - \overrightarrow{A}||$. To summarize, given a permittivity distribution $\epsilon(y)$ and the apex of a hyperbola $[x_0, t_0]$, the depth d of the target is estimated by numerically solving equation (6) using the bisection method. Subsequently, $N(d,\epsilon)$ is evaluated and furthermore used in equation (5) to calculate the arrival times $\mathbf{t} \in \mathbb{R}^n$.

The proposed scheme utilizes numerous hyperbolas and tries to find the optimum $\epsilon(y)$ that simultaneously minimizes $\min_{\epsilon(y)} \sum_{i=1}^{Z} ||\mathbf{t}_i - \mathbf{T}_i||$, where $\mathbf{T}_i \in \mathbb{R}^{n_i}$ and $\mathbf{t}_i \in \mathbb{R}^{n_i}$ represent the measured and predicted arrival times for the ith hyperbola, Z is the total number of the employed hyperbolas and n_i is the number of discretisation points for the ith hyperbola. To further simplify the problem, the permittivity is discretised with K equidistant points and subsequently a cubic interpolation is applied to map ϵ with respect to y in a continuous manner. Therefore, the minimization is re-written as $\min_{\epsilon(k)\ k\in\mathbb{R}^K} \sum_{i=1}^{Z} ||\mathbf{t}_i - \mathbf{T}_i||$ with only K number of unknowns. This is a non-linear and non-convex problem that can be solved using global optimizers. A Particle Swarm Optimisation (PSO) (Kennedy & Eberhart, 1995), with 50 particles and uniform PSO parameters, was proven to be very efficient for reconstructing $\epsilon(y)$, given a sufficient number of measured hyperbolas. The number of equidistant points K is estimated by plotting the Error-K curve. This approach is based on the L-curve method (Hansen, 1992) that tries to balance between accuracy and constraints. Within that context, we choose the K value for which the solution balances accuracy and simplicity. In particular, the minimization is executed multiple times with increasing K until the error starts to converge. The K value is chosen at the earliest point of convergence. Greater K values can potentially result (if a sufficient number of hyperbolas is not present) in unnecessary complicated permittivity structures without increasing the fitting accuracy.

3.2 Numerical experiments

Two numerical 2D case studies (illustrated in Figure 2) are used in this section to evaluate the performance of the proposed scheme. Both models are non-dispersive, non-conductive, and non-magnetic, with a varying permittivity with respect to depth $\epsilon(y)$. Nine perfect electric conductors (PEC) are distributed randomly within a $2\times1\ m^2$ domain. The targets have a cylindrical shape with 5 cm diameter and their main axis is perpendicular to the acquisition line. Measurements are taken every 2 cm along the x-axis using a line source with 1 GHz central frequency. The offset between the transmitter and the receiver is 1 cm. The numerical simulations were executed using gprMax (Warren et al., 2016; Warren et al., 2019), an open source electromagnetic solver that uses a second order (in both space and time) finite-difference time domain (FDTD) method (Yee,

1966). The spatial discretization step of the FDTD grid is $\Delta x = \Delta y = 5$ mm, and the time step Δt is calculated using the Courant limit (Taflove & Hagness, 2000). The boundaries of the domain are truncated using the recursive integration perfectly matched layer (Giannopoulos, 2008).

From Figure 2, it is apparent that even in these clinical clutter-free numerical experiments, the reflections from the layers are very weak and not visible in the measured radargrams. This is due to the smooth transition between the layers that can greatly decrease their reflection coefficient (Bano, 2006; Diamanti et al., 2014). This gives the false impression that a medium is homogeneous when in fact it can be as complex as Model 1 (see Figure 2), with four clear and distinct layers. This is very important when interpreting radargrams from the lunar regolith, where smooth transitions between layers are expected due to space weathering and the reworking of the materials during crater formation.

The proposed scheme and the typical hyperbola-fitting with Dix conversion (Dong, Fang, et al., 2020) were applied to the radargrams shown in Figure 2. In both models, the proposed methodology outperforms conventional hyperbola-fitting, and manages to sufficiently estimate the permittivity profile and the underlying layered structure in an efficient manner (see Figure 2). Small errors observed in Figure 2 can be due to: the linear-path simplification; manual picking of the hyperbolas (Ding et al., 2020); non-accurate time-zero correction (Yelf, 2004); and/or non-ideal targets i.e. $R \neq 0$.

4 Results

The proposed methodology is applied to the high frequency data collected by the Yutu-2 rover at the VK crater during the first two lunar days of the Chang'E-4 mission (Li et al., 2020). During the first two lunar days, the rover followed an irregular path and managed to cover ~ 106 m (Li et al., 2020). The current paper focuses on the first 150 ns of the scan in order to effectively map the shallow layers ($\sim 10 - 12$ m) of the regolith. Based on the results, a revised stratigraphy for the VK crater is proposed that takes into account a previously unseen layered structure within the first ~ 10 m of lunar regolith.

4.1 Lunar penetrating radar results

The radargram was processed using a typical GPR processing pipeline that involves zero-time correction, dewow, time-gain (exponential gain), and background removal (Cassidy, 2009). The resulting B-Scan for the first 150 ns is illustrated in Figure 3 (Li et al., 2020). The overall signal to clutter ratio is substantially higher compared to Chang'E-3 mission (Lai et al., 2019; Li et al., 2020) (potentially due to lack of ilmenite) which results in clear hyperbolic features that can be utilized to deduce the shallow layered structure at the first 10-12 m of the landing site.

Figure 3_A illustrates the resulting permittivity profile using the proposed advanced hyperbola-fitting subject to the hyperbolas shown in Figure 3_B. It is evident that there is a layered structure with four layers in the first 10 m of the regolith. The first and the third layers have low permittivity values while the second and the fourth layers have permittivity up to $\epsilon \approx 10$ (see Figure 3_A). Typical lunar soils have low permittivity values although there are reported high-density lunar samples with relative permittivity up to $\epsilon \approx 10$ (Chung et al., 1970; Olhoeft & Strangway, 1975).

We would like to highlight that current knowledge regarding the permittivity of lunar soils is based primarily on shallow samples brought back to Earth during the Apollo missions. Superficial lunar samples are not representative of deeper layers since they are exposed to space weathering which results in an increased porosity and vitrification (Nash

& Conel, 1973). Moreover, the semi-empirical models tuned for lunar soils are primarily based on those samples (Chung et al., 1970; Frisillo et al., 1975; Carrier et al., 1991; Shkuratov & Bondarenko, 2001), making them unreliable for estimating the dielectric properties of deeper ejecta. Estimation of the dielectric properties of deeper layers is still an ongoing research area that is primarily based on LPR measurements and typical hyperbola-fitting (Dong, Fang, et al., 2020). As shown in section 3, typical hyperbola-fitting is not a reliable approach when applied to inhomogeneous media, and therefore the estimated permittivities using conventional hyperbola-fitting should be used with caution.

4.2 Stratigraphy modeling of the Chang'E-4 landing site

The suggested stratigraphy model is based on the LPR results shown in Figure 3_A and the following premises:

- The thickness of the weathered top soil is $\sim 2.5-7.5$ m (Huang et al., 2018) which is consistent with the average weathering rate (~ 1.5 m/Ga) derived from the Apollo missions (Gou et al., 2021).
- Finsen, VK L and L' craters are the predominant sources of the post-Imbrian ejecta in the VK crater (Huang et al., 2018; Zhang et al., 2020).
- Finsen ejecta at the landing site are estimated via numerical simulations at ~ 35 m (Di et al., 2019).
- Finsen crater was developed before VK L and L' craters (Zhang et al., 2020).
- Finsen crater is within the SPACA region and therefore it is expected that its excavated materials have an increased HCP/LCP ratio (Moriarty & Pieters, 2018). The peak of the Finsen crater has a low HPC/LCP ratio (Ling et al., 2019), nonetheless, the peak of craters is created in a rebound process that uplifts lower materials (Morgan et al., 2016) i.e. materials from the underlying Mg-rich anulus which has low HPC/LPC ratio (Moriarty & Pieters, 2018).
- The ejecta materials from VK L and L' craters have low HCP/LCP ratio (Ling et al., 2019).
- Below the weathered top soil there is an LCP layer down to ~ 13 m (Huang et al., 2018).
- Below the LCP layer there is a thick layer (> 30 m) with high HCP/LCP ratio (Huang et al., 2018).
- There is a clear sharp boundary observed on LPR data (Zhang et al., 2020) at ~ 13 m, most-likely between the LCP and the HCP layer.

The proposed stratigraphy model suggests that the HCP layer overlaying the Imbrian basalts is the ejecta from the Finsen crater (Huang et al., 2018) (and maybe Orientale crater too(Xiao et al., 2021)). This premise is consistent both with the size of this layer (as predicted by numerical simulations (Di et al., 2019)) and with the chemical composition of the Finsen crater (Moriarty & Pieters, 2018). On top of the Finsen ejecta, it is expected to encounter ejecta from Eratosthenian post-Finsen craters. A homogeneous weathered layer with 12 m width as suggested by Zhang et al., 2020 is not consistent with LROC NAC images (Huang et al., 2018) and by the layered structure revealed by the proposed hyperbola-fitting scheme (see Figure 3_A). Therefore, we suggest that the top $\sim 10-12$ m of the landing site consists of ejecta from the VK L and L' craters. This is in good agreement with the LCP content of the VK L and L' craters and with the layered structure illustrated in Figure 3_A. In addition, a 12-13 m regolith indicates a weathering rate of $\sim 3-4$ m/Ga which is twice as fast compared to the ones derived from the Apollo missions (apart from the landing site of Apollo 16) (Gou et al., 2021). The evolution of the post-basaltic flood ejecta of VK crater is shown in Figure 3_C. The ejecta of VK L' (≈ 5.5 m) were deposited on top of the Finsen ejecta at early Eratosthenian. Space weathering degraded the first ~ 1.5 m of the ejecta decreasing its density and consequently its electric permittivity (due to the causal relationship between

permittivity and density (Chung et al., 1970; Olhoeft & Strangway, 1975)). The width of the VK L' regolith is in good agreement with the literature which suggests that rapid weathering is expected at young ejecta, a phenomenon that has also been observed at the Chang'E-3 landing site (Gou et al., 2021). The ejecta from VK L is subsequently deposited on top of the weathered layer creating a top layer with ~ 6 m width. The long weathering process, from early Eratosthenian till now, gave rise to a ~ 3 m of loose lunar soil with low electric permittivity as predicted by Figure 3_A. This is in good agreement with the LROC NAC images (Huang et al., 2018) and also with the average weathering rate (~ 1.5 m/Ga) derived from the Apollo missions (Gou et al., 2021).

5 Conclusions

A novel interpretation tool was described capable of estimating the permittivity profile of the shallow lunar surface using lunar penetrating radar. The validity and the superiority of the suggested scheme compared to typical hyperbola-fitting was demonstrated via a set of numerical experiments that clearly shown that the proposed scheme is capable of reconstructing complicated permittivity profiles using the shape of multiple hyperbolas as the only inputs. The proposed methodology is suitable for any arbitrary one-dimensional permittivity distribution, which makes it an appealing choice for inferring the mechanical and mineralogical properties of lunar regolith. The advanced hyperbola-fitting was applied to the high frequency data collected during the first two lunar days of the Chang'E-4 mission. The resulting permittivity profile indicates a layered structure within the first 10 meters of the regolith. These shallow layers are not visible in the measured radargram due to the smooth boundaries between them, making them undetectable using traditional signal processing approaches. It is argued that the multiple layers detected within the shallow lunar regolith can be the ejecta of the Eratosthenian craters Von K*ármán* L and L', laying on top of the late-Imbrian ejecta of Finsen crater.

Data Availability Statement

The Chang'E-4 Lunar Penetrating Radar data are available from the Data Publishing and Information Service System of China Lunar Exploration Program `http://moon.bao.ac.cn/searchOrder_dataSearchData.search`.

References

Aldo, V. (1996). Ray tracing based on Fermat's principle in irregular grids. *Geophysical Prospecting*, *44*(5), 741-760.

Bano, M. (2006). Effects of the transition zone above a water table on the reflection of GPR waves. *Geophysical Research Letters*, *33*(13).

Boero, F., Fedeli, A., Lanini, M., Maffongelli, M., Monleone, R., Pastorino, M., ... Sansalone, A. (2018). Microwave tomography for the inspection of wood materials: Imaging system and experimental results. *IEEE Transactions on Microwave Theory and Techniques*, *66*(7), 3497-3510.

Carrier, W. D., Olhoeft, G. R., & Mendell, W. (1991). Physical properties of the lunar surface. *Lunar Sourcebook*, 522-530.

Cassidy, N. J. (2009). Chapter 5 - ground penetrating radar data processing, modelling and analysis. In H. M. Jol (Ed.), *Ground penetrating radar theory and applications* (p. 141-176). Amsterdam: Elsevier.

Chung, D. H., Westphal, W. B., & Simmons, G. (1970). Dielectric properties of Apollo 11 lunar samples and their comparison with Earth materials. *Journal of Geophysical Research*, *75*(13), 6524-6531.

Conyers, L. B. (2004). Ground penetrating radar for archaeology. Walnut Creek, CA, USA: AltaMira Press.

Daniels, D. J. (2004). *Ground penetrating radar*. U.K.:Institution of Engineering and Technology.

Di, K., Zhu, M. H., Yue, Z., Lin, Y., Wan, W., Liu, Z., ... Xue, B. (2019). Topographic evolution of Von Kármán crater revealed by the lunar rover Yutu-2. *Geophysical Research Letters*, *46*, 764-770.

Diamanti, N., Annan, A. P., & Redman, J. D. (2014). Impact of gradational electrical properties on gpr detection of interfaces. In *Proceedings of the 15th international conference on ground penetrating radar* (p. 529-534).

Ding, C., Xiao, Z., Su, Y., & Cui, J. (2020). Hyperbolic reflectors determined from peak echoes of ground penetrating radar. *Icarus*, 114280.

Dix, C. H. (1955). Seismic velocities from surface measurements. *Geophysics*, *20*, 68-86.

Dong, Z., Fang, G., Zhao, D., Zhou, B., Gao, Y., & Ji, Y. (2020). Dielectric properties of lunar subsurface materials. *Geophysical Research Letters*, *47*.

Dong, Z., Feng, X., Zhou, H., Liu, C., Zeng, Z., Li, J., & Liang, W. (2020). Properties analysis of lunar regolith at Chang'E-4 landing site based on 3d velocity spectrum of lunar penetrating radar. *Remote Sensing*, *12*, 629.

Fa, W. (2020). Bulk density of the lunar regolith at the Chang'E-3 landing site as estimated from lunar penetrating radar. *Earth and Space Science*, *7*(0).

Feng, X., Sato, M., & Liu, C. (2012). Subsurface imaging using a handheld gpr md system. *IEEE Geoscience and Remote Sensing Letters*, *9*(4), 659-662.

Frisillo, A. L., Olhoeft, G. R., & Strangway, D. W. (1975). Effects of vertical stress, temperature and density on the dielectric properties of lunar samples 72441, 12, 15301, 38 and a terrestrial basalt. *Earth and Planetary Science Letters*, *24*, 345-356.

Giannakis, I., Giannopoulos, A., & Warren, C. (2016). A realistic FDTD numerical modeling framework of ground penetrating radar for landmine detection. *IEEE Journal of Selected Topics in Applied Earth Observations and Remote Sensing*, *9*(1), 37-51.

Giannakis, I., Giannopoulos, A., & Warren, C. (2019). A machine learning-based fast-forward solver for ground penetrating radar with application to full-waveform inversion. *IEEE Transactions on Geoscience and Remote Sensing*, *57*(7), 4417-4426.

Giannakis, I., Giannopoulos, A., & Warren, C. (2020). A machine learning scheme for estimating the diameter of reinforcing bars using ground penetrating radar. *IEEE Geoscience and Remote Sensing Letters*, 1-5.

Giannopoulos, A. (2008). An improved new implementation of complex frequency shifted PML for the FDTD method. *IEEE Transactions on Antennas and Propagation*, *56*(9), 2995-3000.

Gou, S., Di, K., Yue, Z., Liu, Z., He, Z., Xu, R., ... Liu, J. (2020). Forsteritic olivine and magnesium-rich orthopyroxene materials measured by Chang'E-4 rover. *Icarus*, *345*, 113776.

Gou, S., Yue, Z., Di, K., Cai, Z., Liu, Z., & Niu, S. (2021). Absolute model age of lunar finsen crater and geologic implications. *Icarus*, *354*, 114046.

Hansen, P. C. (1992). Analysis of discrete ill-posed problems by means of the l-curve. *SIAM Rev.*, *34*, 561-580.

Hickson, D., Boivin, A., Daly, M. G., Ghent, R., Nolan, M. C., Tait, K., ... Tsai, C. A. (2018). Near surface bulk density estimates of neas from radar observations and permittivity measurements of powdered geologic material. *Icarus*, *306*.

Hu, X., Ma, P., Yang, Y., Zhu, M., Jiang, T., Lucey, P. G., & et al. (2019). Mineral abundances inferred from insitu reflectance measurements of Chang'E-4 landing site in South-Pole Atkins. *Geophysical Research Letters.*, *46*, 9439-9447.

Huang, J., Xiao, Z., Flahaut, J., Martinot, M., Head, J., Xiao, X., & et al. (2018). Geological characteristics of Von Kármán crater, northwestern South Pole-

Aitken basin: Chang'E-4 landing site region. *Journal of Geophysical Research: Planets*, *123*, 1684-1700.

Ivanov, M. A., Hiesinger, H., van derBogert, C. H., Orgel, C., Pasckert, J. H., & Head, J. W. (2018). Geologic history of the northern portion of the South Pole-Aitken basin on the Moon. *Journal of Geophysical Research: Planets*, *123*, 2585–2612.

James, P. B., Smith, D. E., Byrne, P. K., Kendall, J. D., Melosh, H. J., & Zuber, M. T. (2019). Deep structure of the lunar South Pole-Aitken basin. *Geophysical Research Letters*, *46*, 5100-5106.

Jolliff, B. L., Gillis, J. J., Haskin, L. A., Korotev, R. L., & Wieczorek, M. A. (2000). Major lunar crustal terranes: Surface expressions and crust-mantle origin. *Journal of Geophysical Research*, *105*, 4197-4216.

Kennedy, J., & Eberhart, R. (1995). Particle swarm optimization. *in Proc. IEEE Int. Conf. Neural Netw.*, *4*, 1942-1948.

Khan, A. (2002). An inquiry into the lunar interior: A nonlinear inversion of the Apollo lunar seismic data. *Journal of Geophysical Research*, *107*, 3.1-3.18.

Lai, J., Xu, Y., Bugiolacchi, R., Meng, X., Xiao, L., Xie, M., ... Xu, L. (2020). First look by the Yutu-2 rover at the deep subsurface structure at the lunar farside. *Nature Communications*, *11*, 3426.

Lai, J., Xu, Y., Zhang, X., Xiao, L., Yan, Q., Meng, X., ... D., Z. (2019). Comparison of dielectric properties and structure of lunar regolith at Chang'e-3 and Chang'e-4 landing sites revealed by ground-penetrating radar. *Geophysical Research Letters*, *46*.

Lauro, S. E., Pettinelli, E., Caprarelli, G., Guallini, L., Rossi, A. P., Mattei, E., ... R, O. (2020). Multiple subglacial water bodies below the south pole of Mars unveiled by new MARSIS data. *Nature Astronomy*.

Li, C., Liu, D., Liu, B., Ren, X., Liu, J., He, Z., ... Ouyang Z, Z. (2019). Chang'e-4 initial spectroscopic identification of lunar far-side mantle-derived materials. *Nature*, *569*, 378-382.

Li, C., Su, Y., Pettinelli, E., Xing, S., Ding, C., Liu, J., ... Zhang, H. (2020). The moon's farside shallow subsurface structure unveiled by Chang'E-4 lunar penetrating radar. *Science Advances*, *6*(9).

Li, C., Xing, S., Lauro, S. E., Su, Y., Dai, S., Feng, J., ... Pettinelli, E. (2018). Pitfalls in GPR data interpretation: False reflectors detected in lunar radar cross sections by Chang'E-3. *IEEE Transactions on Geoscience and Remote Sensing*, *56*(3), 1325-1335.

Li, J., Liu, C., Zeng, Z., & Chen, L. (2015). GPR signal denoising and target extraction with the CEEMD method. *IEEE Geoscience and Remote Sensing Letters*, *12*(8), 1615-1619.

Lin, H., Lin, Y., Yang, W., He, Z., Hu, S., Wei, R., Y. Xu, ... Zou, Y. (2020). New insight into lunar regolith forming processes by the lunar rover Yutu-2. *Geophysical Research Letters*, *47*.

Ling, Z., Qiao, L., Liu, C., Cao, H., Bi, X., Lu, X., ... Liu, J. (2019). Composition, mineralogy and chronology of mare basalts and non-mare materials in Von Kármán crater: Landing site of the Chang'E4 mission. *Planetary and Space Science*, *179*, 104741.

Lu, Y., Wu, Y., Michael, G. G., Ma, J., Cai, W., & Qin, N. (2021). Chronological sequence of chang'e-4 landing zone within von kármán crater. *Icarus*, *354*, 114086.

Matsunaga, T., Ohtake, M., Haruyama, J., Ogawa, Y., Nakamura, R., Yokota, Y., ... Otake, H. (2008). Discoveries on the lithology of lunar crater central peaks. *Geophysical Research Letters*, *35*, L23201.

Meles, G. A., Van der Kruk, J., Greenhalgh, S. A., Ernst, J. R., Maurer, H., & Green, A. G. (2010). A new vector waveform inversion algorithm for simultaneous updating of conductivity and permittivity parameters from combination

crosshole/borehole-to-surface GPR data. *IEEE Transactions on Geoscience and Remote Sensing*, *48*(9), 3391-3407.

Mertens, L., Persico, R., Matera, L., & Lambot, S. (2016). Automated detection of reflection hyperbolas in complex GPR images with no a priori knowledge on the medium. *IEEE Transactions on Geoscience and Remote Sensing*, *54*(1), 580-596.

Morgan, J. V., Gulick, P. S., Bralower, T., ..., & Zylberman, W. (2016). The formation of peak rings in large impact craters. *Science*, *354*, 878-882.

Moriarty, D. P., & Pieters, C. M. (2018). The character of South Pole-Aitken Basin: Patterns of surface and subsurface composition. *Journal of Geophysical Research: Planets*, *123*, 729-747.

Moriarty, D. P., Pieters, C. M., & Isaacson, P. J. (2013). Compositional heterogeneity of central peaks within the South Pole-Aitken Basin. *Journal of Geophysical Research: Planets*, *118*, 2310-2322.

Nash, D. B., & Conel, J. E. (1973). Vitrification darkening of rock powders: implications for optical properties of the lunar surface. *The Moon*, *8*(3), 346-364.

Olhoeft, G. R., & Strangway, D. W. (1975). Dielectric properties of the first 100 meters of the moon. *Lunar Sourcebook*, *24*.

Paskert, J. H., Hiesinger, H., & van der Bogert, C. H. (2018). Lunar far side volcanism in and around the South Pole–Aitken basin. *Icarus*, *299*, 538-562.

Potter, R. W. K., Collins, G. S., Kiefer, W. S., McGovern, P. J., & Kring, D. A. (2012). Constraining the size of the South Pole-Aitken basin impact. *Icarus*, *220*, 730-743.

Shkuratov, Y. G., & Bondarenko, N. Y. (2001). Regolith layer thickness mapping of the Moon by radar and optical data. *Icarus*, *149*, 329-338.

Stopar, J. D., Robinson, M. S., Barnouin, O. S., McEwen, A. S., Speyerer, E. J., Henriksen, M. R., & Sutton, S. S. (2017). Relative depths of simple craters and the nature of the lunar regolith. *Icarus*, *298*, 34 - 48.

Taflove, A., & Hagness, S. C. (2000). *Computational electrodynamics: The finite-difference time-domain method*. Norwood, MA, USA:Artech House.

Tang, Z., Liu, J., Wang, X., Ren, X., Chen, W., Yan, W., & et al. (2020). Physical and mechanical characteristics of lunar soil at the Chang'E-4 landing site. *Geophysical Research Letters.*, *47*, 1-8.

Tompkins, S., & Pieters, C. M. (1999). Mineralogy of the lunar crust: Results from Clementine. *Meteoritics & Planetary Science*, *34*, 25-41.

Wai-Lok Lai, W., Dérobert, X., & Annan, P. (2018). A review of ground penetrating radar application in civil engineering: A 30-year journey from locating and testing to imaging and diagnosis. *NDT E International*, *96*, 58 - 78.

Warren, C., Giannopoulos, A., & Giannakis, I. (2016). gprMax: Open source software to simulate electromagnetic wave propagation for ground penetrating radar. *Computer Physics Communications*, *209*, 163-170.

Warren, C., Giannopoulos, A., Gray, A., Giannakis, I., Patterson, A., Wetter, L., & Hamrah, A. (2019). A CUDA-based GPU engine for gprMax: Open source FDTD electromagnetic simulation software. *Computer Physics Communications*, *237*, 208 - 218.

Wieczorek, M. A., Neumann, G. A., Nimmo, F., Kiefer, W. S., Taylor, G. J., Melosh, H. J., ... Zuber, M. T. (2013). The crust of the Moon as seen by GRAIL. *Science*, *339*, 671-675.

Williams, R. M., Ray, L. E., Lever, J. H., & Burzynski, A. M. (2014). Crevasse detection in ice sheets using ground penetrating radar and machine learning. *IEEE Journal of Selected Topics in Applied Earth Observations and Remote Sensing*, *7*(12), 4836-4848.

Xiao, Z., Ding, C., Xie, M., Cai, Y., Cui, J., Zhang, K., & Wang, J. (2021). Ejecta from the orientale basin at the chang'e-4 landing site. *Geophysical Research Letters*.

Yamamoto, S. R., Nakamura, R., Matsunaga, T., Ogawa, Y., Ishihara, Y., Morota, T., ... Junuchi, H. (2010). Possible mantle origin of olivine around lunar impact basins detected by SELENE. *Nature Geosciences*, *3*, 533-536.

Yee, K. (1966). Numerical solution of initial boundary value problems involving Maxwell's equations in isotropic media. *IEEE Transactions on Antennas and Propagation*, *14*(3), 302-307.

Yelf, R. (2004). Where is true time zero ? In *Proceedings of the tenth international conference on grounds penetrating radar, 2004. gpr 2004.* (Vol. 1, p. 279-282).

Yue, Z., Yang, M., Jia, M., Michael, G., Di, K., Gou, S., & Liu, J. (2020). Refined model age for orientale basin derived from zonal crater dating of its ejecta. *Icarus*, *346*, 113804.

Zhang, L., Li, J., Zeng, Z., Xu, Y., Liu, C., & Chen, S. (2020). Stratigraphy of the Von Kármán crater based on Chang'E-4 lunar penetrating radar data. *Geophysical Research Letters*, *47*.

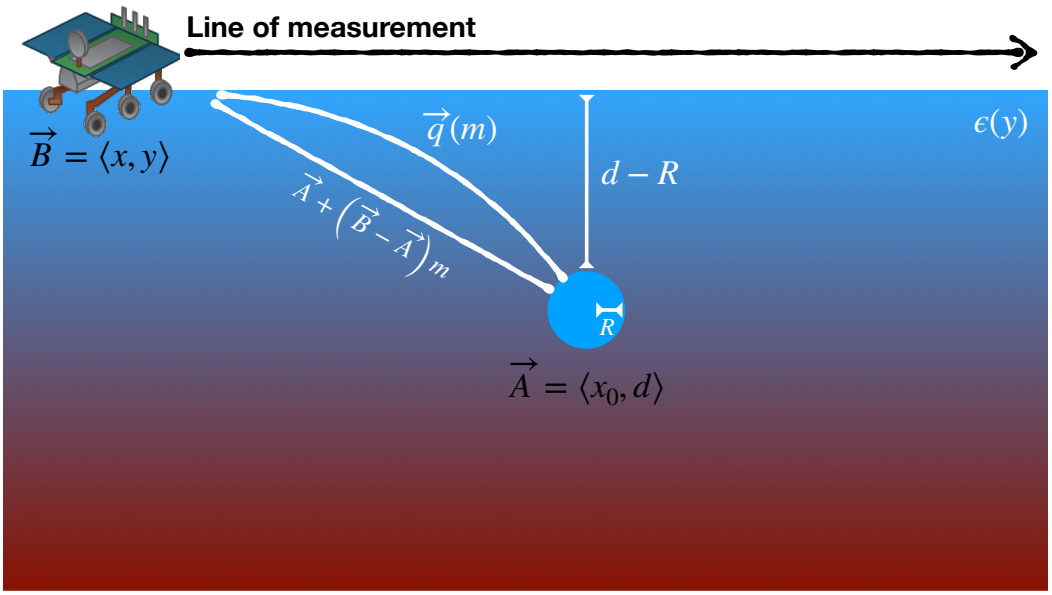

Figure 1. A simple scenario investigating a cylindrical target with radius R buried in a half-space subject to a 1D electric permittivity distribution with respect to depth $\epsilon(y)$. The vector positions of the center of the target and the antenna are $\vec{A} = \langle x_0, d \rangle$ and $\vec{B} = \langle x, y \rangle$ respectively. The distance between the antenna and the surface of the target equals $||\vec{A} - \vec{B}|| - R$. For both lunar and Earth applications, the permittivity often increases with depth and therefore the velocity is expected to decrease. Due to that, the wave will follow a path similar to the parametric curve $q(m)$ with $m \in [0 - 1]$. The parametric equation of the line that connects the point of measurement to the centre of the target is given by $\vec{A} + \left(\vec{B} - \vec{A}\right) m$.

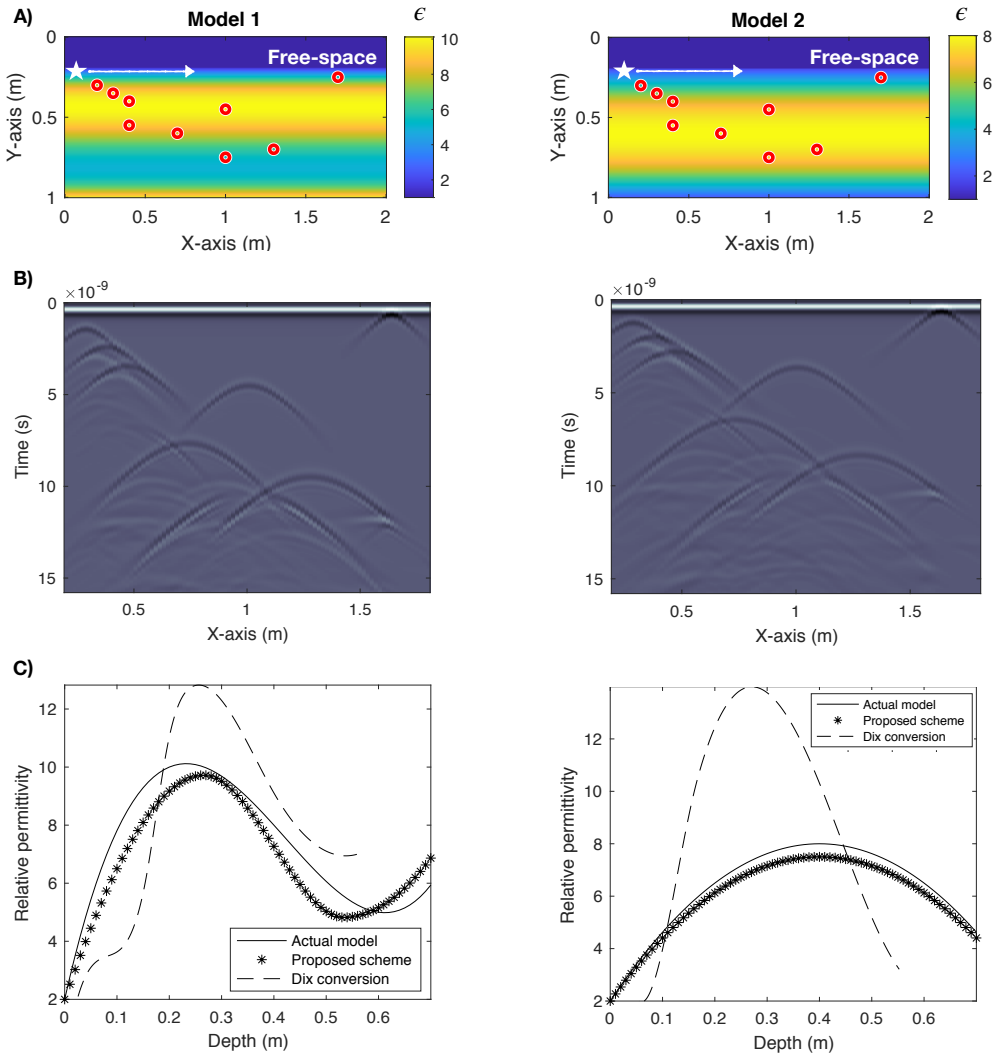

Figure 2. A) The investigated numerical experiments. Nine cylindrical targets are buried in two media with varying permittivity with respect to depth. Measurements are taken every 2 cm (from left to right) using a ground-coupled line source (white star) with 1 GHz central frequency. B) Resulting B-Scans. It is evident that due to the smooth boundaries between the layers, no reflections are visible on the resulting radargrams. The shapes of the hyperbolas are the only features that can be used to infer the permittivity profile. C) The resulting permittivity profile for the models shown in Figure 2_A.

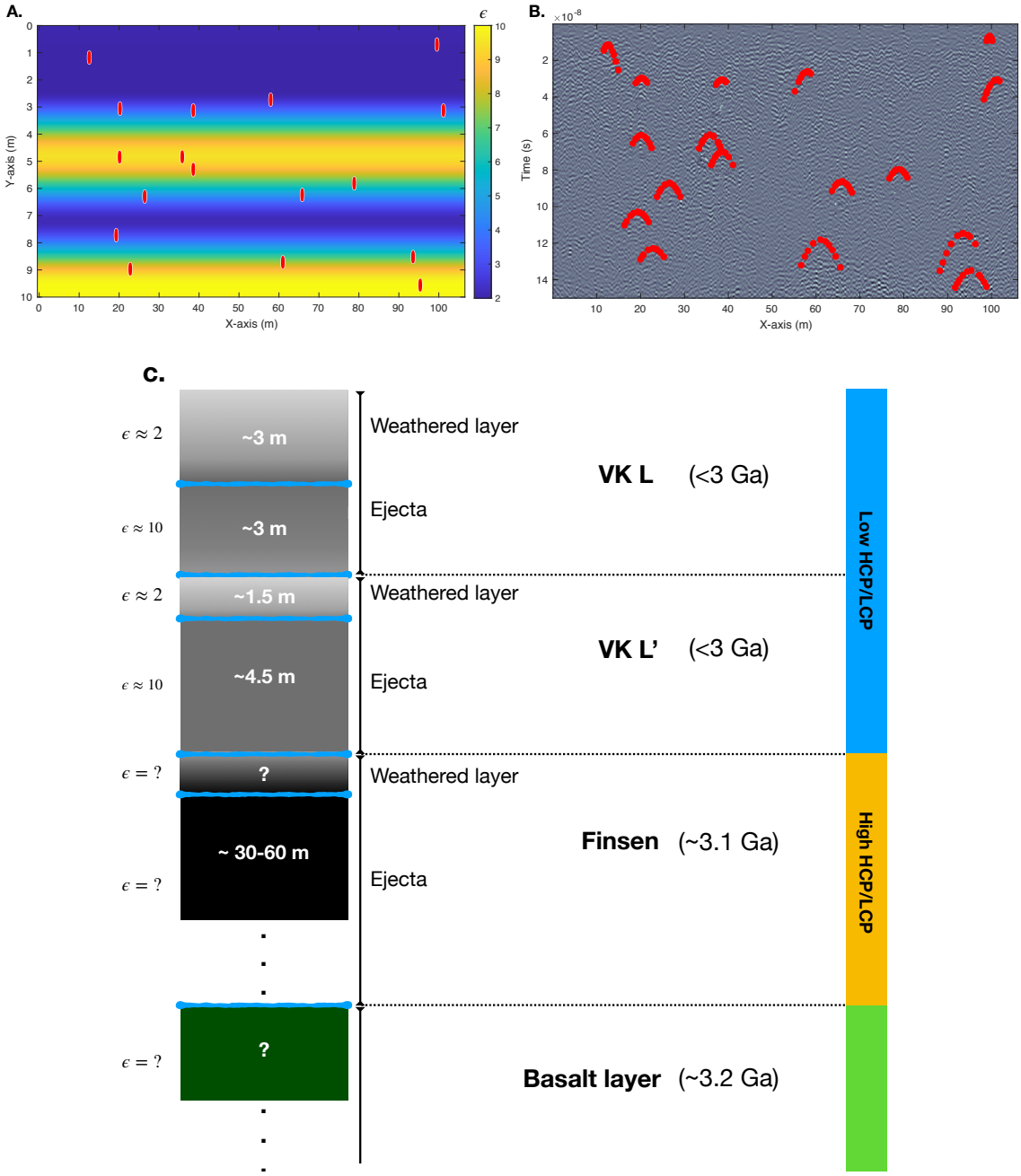

Figure 3. A) The resulting permittivity profile $\epsilon(y)$ at the landing site of Chang'E-4 mission using the advanced hyperbola fitting. The coordinates of the investigated targets are illustrated with red dots. B) The fitted hyperbolas subject to the permittivity profile shown in Figure 3_A. C) The proposed stratigraphy model for the Chang'E-4 landing site. The first $\sim$ 6 m consists of a top weathered layer overlaying the ejecta from VK L crater. Below that, is a low permittivity layer that corresponds to the weathered ejecta of the VK L' crater. The VK L' ejecta extends to $\sim$ 12 m depth, where the Finsen and Alder ejecta lay on top of the Imbrian basaltic layer. Dates are based on (Lu et al., 2021) and the chemical composition on (Huang et al., 2018).